Journal of Computational Physics **181,** 260–279 (2002)
doi:10.1006/jcph.2002.7123

Direct Simulation of the Motion of Neutrally Buoyant Circular Cylinders in Plane Poiseuille Flow

Tsorng-Whay Pan and Roland Glowinski

Department of Mathematics, University of Houston, Houston, Texas 77204-3476
E-mail: pan@math.uh.edu

Received October 29, 2001; revised June 3, 2002

In this article we discuss the generalization of a Lagrange multiplier-based fictitious domain method to the simulation of the motion of neutrally buoyant particles in a Newtonian fluid. Then we apply it to study the migration of neutrally buoyant circular cylinders in plane Poiseuille flow of a Newtonian fluid by direct numerical simulation. The Segré–Silberberg effect is found for the cases with one and several circular cylinders. In general, it is believed that the migration away from the center of the channel is due to an effect of the curvature of velocity profile. Via direct numerical simulation, we find that this effect is not weakened by the presence of many particles, but by the collisions among the particles. Experiments and simulations for hundreds of circular cylinder cases show that particles concentrate in the central region where the shear rate is low. A power law associated with the horizontal velocity of the mixture of fluid/particles is also presented.

Key Words: particulate flow; solid–liquid flow; neutrally buoyant particle; fictitious domain method; distributed Lagrange multiplier; operator splitting; finite element; power law.

1. INTRODUCTION

The problem of particle motions in shear flows is crucially important in many engineering fields such as the handling of a fluid–solid mixture in slurry, colloid, and fluidized bed. The experiments of Segré and Silberberg [23, 24] have had a large influence on fluid mechanics studies of migration and lift of particles. They studied the migration of dilute suspensions of neutrally buoyant spheres in pipe flow at Reynolds numbers between 2 and 700. The particles migrate away from the wall and centerline and accumulate at about 0.6 of a pipe radius from the centerline. Karnis *et al.* [16] verified the same phenomenon and observed that particles migrate faster for larger flow rate and closer to the axis for the larger rigid

0021-9991/02 $35.00

sphere. The "anomalous" motion observed is attributed to the nonlinear effect of inertia. Comprehensive reviews of experimental and theoretical works have been given by Brenner [4], Cox and Mason [6], Leal [17], and Feuillebois [9].

Direct numerical simulations have been used for understanding particle motion in shear flows. Feng *et al.* [8] investigated the motion of neutrally buoyant and nonneutrally buoyant circular particles in plane Couette and Poiseuille flows using a finite element method and obtained qualitative agreement with the results of perturbation theories and of experiments. Morris and Brady [20] performed numerical studies on the influence of particle buoyancy in pressure-driven flow of a suspension when inertia is neglected and compared with experimental results. They found that shear-induced migration in Stokes flows competes with buoyancy effects and concluded that the flow behavior depends strongly on both the bulk particle volume fraction and the dimensionless gravitational parameter, but only weakly on the the dimensionless channel width. Huang and Joseph [14] found, via numerical simulation, that at moderate Reynolds numbers in a pressure-driven plane Poiseuille flow, shear thinning causes neutrally buoyant particles (for the case with 56 circular cylinders) to migrate away from centerline, creating a particle-free zone, which increases the amount of shearing thinning. In a visco-elastic fluid with shear thinning, particle migrates toward either the centerline or the walls, creating an annular particle-free zone at intermediate radii. Inamuro *et al.* [15] used the lattice Boltzmann method to study the motions of neutrally buoyant circular disks in a pressure-driven plane Poiseuille flow. The Segré–Silberberg effect was found. They found that the equilibrium position of the particle is closer to the wall as the Reynolds number increases from about 12 to 96; but it moves away from the wall as either the diameter of the disk or the length of the channel is increased.

In this article, we discuss the generalization of a *distributed Lagrange multiplier/fictitious domain method* (DLM/FD) for the numerical simulation of particulate flow (see [12, 13]) to the case where the particles are neutrally buoyant. Via the DLM/FD method, we do not need to compute the hydrodynamical forces explicitly in the simulation since the interaction between the fluid and the particles is implicitly modeled by the global variational formulation at the foundation of the methodology employed here. We can also avoid generating boundary fitted grids for different positions of the particles; indeed one just needs a simple structured grid and the geometrical relation between the particles and the grid. This DLM/FD method has been successfully applied, in [12] and [13], to simulate particulate flow in two and three dimensions with the number of nonneutrally buoyant particles on the order of 10^3–10^4 in 2-D and 10^2–10^3 in 3-D. We then applied this approach to study, via direct numerical simulation, the migration of neutrally buoyant particles in a pressure-driven flow of an incompressible viscous Newtonian fluid. The Segré–Silberberg effect is found for the cases with few cylinders. In general, it is believed that the migration away from the center of the channel is due to an effect of the curvature of velocity profile (see [2]). Via direct numerical simulation, we found that this effect is not weakened by the presence of many particles, but in fact by the collisions between the particles. Experiments and simulations for hundreds of circular cylinder cases show that particles concentrate in the central region where the shear rate is low. A power law associated with the horizontal velocity of mixture of the fluid and particles is also presented.

The content of this article is as follows: In Section 2 we introduce a fictitious domain formulation of the model problem associated with the neutrally buoyant particle cases; then in Section 3 we discuss the time and space discretizations and in Section 4 we present and

discuss the numerical results of cases with one, several, and several hundreds of neutrally buoyant particles.

2. A FICTITIOUS DOMAIN FORMULATION OF THE MODEL PROBLEM

Let $\Omega \subset \mathbb{R}^2$ be a rectangular region (three-dimensional cases can be treated by a similar approach). We suppose that Ω is filled with a *Newtonian viscous incompressible* fluid (of density ρ_f and viscosity μ_f) and contains a moving neutrally buoyant rigid particle B centered at $\mathbf{G} = \{G_1, G_2\}^t$ of density ρ_f, as shown in Figure 1; the flow is modeled by the *Navier–Stokes equations* and the motion of B is described by the *Euler–Newton's equations*. We define

$$W_{0,p} = \{\mathbf{v} \mid \mathbf{v} \in (H^1(\Omega))^2, \mathbf{v} = \mathbf{0} \text{ on the top and bottom of } \Omega \text{ and } \mathbf{v} \text{ is periodic in the } x_1 \text{ direction}\},$$

$$L_0^2 = \left\{q \mid q \in L^2(\Omega), \int_\Omega q\, d\mathbf{x} = 0,\right\},$$

$$\Lambda_0(t) = \left\{\boldsymbol{\mu} \mid \boldsymbol{\mu} \in (H^1(B(t)))^2, \langle \boldsymbol{\mu}, \mathbf{e_i}\rangle_{B(t)} = 0, i = 1, 2, \langle \boldsymbol{\mu}, \overrightarrow{Gx}^{\perp}\rangle_{B(t)} = 0\right\}$$

with $\mathbf{e}_1 = \{1, 0\}^t, \mathbf{e}_2 = \{0, 1\}^t, \overrightarrow{Gx}^{\perp} = \{-(x_2 - G_2), x_1 - G_1\}^t$, and $\langle \cdot, \cdot \rangle_{B(t)}$ an inner product on $\Lambda_0(t)$, which can be the standard inner product on $(H^1(B(t)))^2$ (see [13], Sect. 5, for further information on the choice of $\langle \cdot, \cdot \rangle_{B(t)}$). Then the fictitious domain formulation with distributed Lagrange multipliers for flow around a freely moving neutrally buoyant particle (see [12, 13] for detailed discussion of nonneutrally buoyant cases) is as follows

For a.e. $t > 0$, find $\mathbf{u}(t) \in W_{0,p}$, $p(t) \in L_0^2$, $\mathbf{V_G}(t) \in \mathbb{R}^2$, $\mathbf{G}(t) \in \mathbb{R}^2$, $\omega(t) \in \mathbb{R}$, $\boldsymbol{\lambda}(t) \in \Lambda_0(t)$ such that

$$\rho_f \int_\Omega \left[\frac{\partial \mathbf{u}}{\partial t} + (\mathbf{u} \cdot \boldsymbol{\nabla})\mathbf{u}\right] \cdot \mathbf{v}\, d\mathbf{x} + 2\mu_f \int_\Omega \mathbf{D}(\mathbf{u}) : \mathbf{D}(\mathbf{v})\, d\mathbf{x} - \int_\Omega p \boldsymbol{\nabla} \cdot \mathbf{v}\, d\mathbf{x} - \langle \boldsymbol{\lambda}, \mathbf{v}\rangle_{B(t)}$$
$$= \rho_f \int_\Omega \mathbf{g} \cdot \mathbf{v}\, d\mathbf{x} + \int_\Omega \mathbf{F} \cdot \mathbf{v}\, d\mathbf{x}, \quad \forall \mathbf{v} \in W_{0,p}, \tag{1}$$

$$\int_\Omega q \boldsymbol{\nabla} \cdot \mathbf{u}(t)\, d\mathbf{x} = 0, \quad \forall q \in L^2(\Omega), \tag{2}$$

$$\langle \boldsymbol{\mu}, \mathbf{u}(t)\rangle_{B(t)} = 0, \quad \forall \boldsymbol{\mu} \in \Lambda_0(t), \tag{3}$$

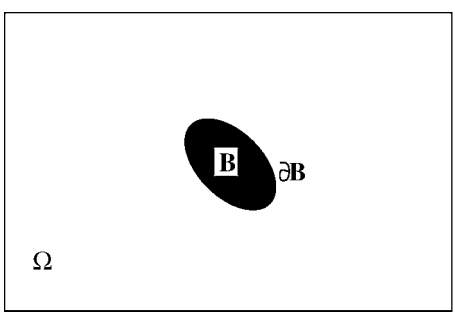

FIG. 1. An example of a two-dimensional flow region with one rigid body.

$$\frac{d\mathbf{G}}{dt} = \mathbf{V_G}, \tag{4}$$

$$\mathbf{V_G}(0) = \mathbf{V_G^0}, \quad \omega(0) = \omega^0, \quad \mathbf{G}(0) = \mathbf{G}^0 = \left\{G_1^0, G_2^0\right\}^t, \tag{5}$$

$$\mathbf{u}(\mathbf{x}, 0) = \bar{\mathbf{u}}_0(\mathbf{x}) = \begin{cases} \mathbf{u}_0(\mathbf{x}), & \forall \mathbf{x} \in \Omega \backslash \overline{B(0)}, \\ \mathbf{V_G^0} + \omega^0 \left\{-\left(x_2 - G_2^0\right), x_1 - G_1^0\right\}^t, & \forall \mathbf{x} \in \overline{B(0)}, \end{cases} \tag{6}$$

where $\mathbf{u}$ and p denote velocity and pressure, respectively, $\boldsymbol{\lambda}$ is a Lagrange multiplier, $\mathbf{D}(\mathbf{v}) = (\boldsymbol{\nabla}\mathbf{v} + \boldsymbol{\nabla}\mathbf{v}^t)/2$, $\mathbf{g}$ is gravity, $\mathbf{F}$ is the pressure gradient pointing in the x_1 direction, $\mathbf{V_G}$ is the *translation velocity* of the particle B, and ω is the *angular velocity* of B. We suppose that the *no-slip* condition holds on ∂B. We also use, if necessary, the notation $\phi(t)$ for the function $\mathbf{x} \to \phi(\mathbf{x}, t)$.

Remark 1. The hydrodynamical forces and torque imposed on the rigid body by the fluid are built in (1)–(6) implicitly (see [12, 13] for details); thus we do not need to compute them explicitly in the simulation. Since in (1)–(6) the flow field is defined on the entire domain Ω, it can be computed with a simple structured grid.

Remark 2. In (3), the rigid body motion in the region occupied by the particle is enforced via Lagrange multipliers $\boldsymbol{\lambda}$. To recover the translation velocity $\mathbf{V_G}(t)$ and the angular velocity $\omega(t)$, we solve the following equations

$$\begin{aligned} \left\langle \mathbf{e}_i, \mathbf{u}(t) - \mathbf{V_G}(t) - \omega(t)\overrightarrow{G\mathbf{x}}^{\perp} \right\rangle_{B(t)} &= 0, \quad \text{for } i = 1, 2, \\ \left\langle \overrightarrow{G\mathbf{x}}^{\perp}, \mathbf{u}(t) - \mathbf{V_G}(t) - \omega(t)\overrightarrow{G\mathbf{x}}^{\perp} \right\rangle_{B(t)} &= 0. \end{aligned} \tag{7}$$

Remark 3. In (1), $2\int_\Omega \mathbf{D}(\mathbf{u}) : \mathbf{D}(\mathbf{v})\, d\mathbf{x}$ can be replaced by $\int_\Omega \boldsymbol{\nabla}\mathbf{u} : \boldsymbol{\nabla}\mathbf{v}\, d\mathbf{x}$ since $\mathbf{u}$ is divergence free and in $W_{0,p}$. Also the gravity $\mathbf{g}$ in (1) can be absorbed into the pressure term.

3. SPACE APPROXIMATION AND TIME DISCRETIZATION

Concerning the *space approximation* of problems (1)–(6) by a finite element method, we shall proceed as follows:

We use P_1-*iso*-P_2 and P_1 finite elements for the velocity field and pressure, respectively (like in Bristeau *et al.* [5]). More precisely with h a *space discretization step* we introduce a finite element triangulation $\mathcal{T}_h$ of $\bar{\Omega}$ and then $\mathcal{T}_{2h}$ a triangulation twice coarser (in practice we should construct $\mathcal{T}_{2h}$ first and then $\mathcal{T}_h$ by joining the midpoints of the edges of $\mathcal{T}_{2h}$, dividing thus each triangle of $\mathcal{T}_{2h}$ into four similar subtriangles as shown in Fig. 2).

We approximate then $W_{0,p}$, L^2, and L_0^2 by the following finite-dimensional spaces

$$\begin{aligned} W_{0,h} = \{\mathbf{v}_h \mid \mathbf{v}_h \in (C^0(\bar{\Omega}))^2, \mathbf{v}_h|_T \in P_1 \times P_1, \forall T \in \mathcal{T}_h, \mathbf{v}_h = \mathbf{0} \text{ on the top and bottom} \\ \text{of } \Omega \text{ and } \mathbf{v} \text{ is periodic at } \boldsymbol{\Gamma} \text{ in the } x_1 \text{ direction}\}, \end{aligned} \tag{8}$$

$$L_h^2 = \{q_h \mid q_h \in C^0(\bar{\Omega}), q_h|_T \in P_1, \forall T \in \mathcal{T}_{2h}, q_h \text{ is periodic at } \Gamma \text{ in the } x_1 \text{ direction}\}, \tag{9}$$

and

$$L_{0,h}^2 = \left\{q_h \mid q_h \in L_h^2, \int_\Omega q_h\, d\mathbf{x} = 0\right\}, \tag{10}$$

respectively; in (8)–(10), P_1 is the space of polynomials in two variables of degree ≤ 1.

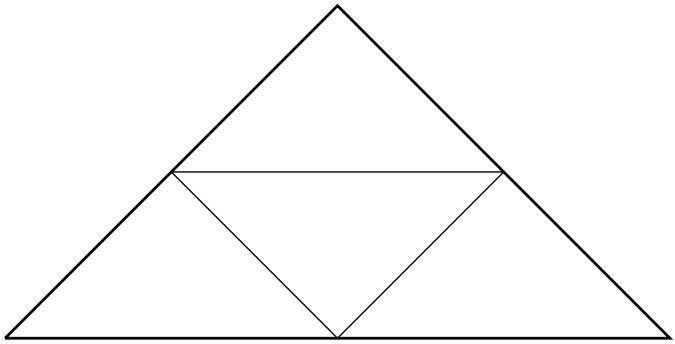

FIG. 2. Subdivision of a triangle of $\mathcal{T}_{2h}$.

A finite-dimensional space approximating $\Lambda_0(t)$ is defined as follows: Let $\{\mathbf{x}_i\}_{i=1}^N$ be a set of points covering $\overline{B(t)}$ (see Fig. 3, for example); we define then

$$\Lambda_h(t) = \left\{ \boldsymbol{\mu}_h \mid \boldsymbol{\mu}_h = \sum_{i=1}^{N} \boldsymbol{\mu}_i \delta(\mathbf{x} - \mathbf{x}_i),\ \boldsymbol{\mu}_i \in \mathbb{R}^2, \forall i = 1, \ldots, N \right\}, \tag{11}$$

where $\delta(\cdot)$ is the Dirac measure at $\mathbf{x} = 0$. Then, instead of the scalar product of $(H^1(B(t)))^2$

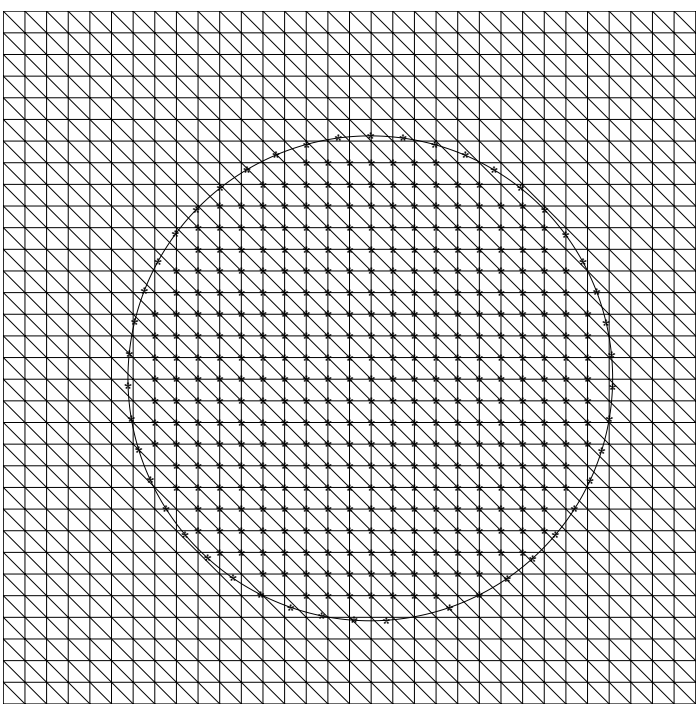

FIG. 3. An example of a set of collocation points chosen for enforcing the rigid body motion inside the disk and at its boundary.

we shall use $\langle \cdot, \cdot \rangle_{B_h(t)}$ defined by

$$\langle \boldsymbol{\mu}_h, \mathbf{v}_h \rangle_{B_h(t)} = \sum_{i=1}^{N} \boldsymbol{\mu}_i \cdot \mathbf{v}_h(\mathbf{x}_i), \quad \forall \boldsymbol{\mu}_h \in \Lambda_h(t), \quad \mathbf{v}_h \in W_{0,h}. \tag{12}$$

Then we approximate $\Lambda_0(t)$ by

$$\Lambda_{0,h}(t) = \left\{ \mu_h \mid \mu_h \in \Lambda_h(t), \langle \mu_h, \mathbf{e}_i \rangle_{B_h(t)} = 0, i = 1, 2, \left\langle \mu_h, \overrightarrow{Gx}^{\perp} \right\rangle_{B_h(t)} = 0 \right\}. \tag{13}$$

The inner product $\langle \cdot, \cdot \rangle_{B_h(t)}$ in (12) makes little sense for the continuous problem, but it is meaningful for the discrete problem; it amounts to forcing the rigid body motion of $B(t)$ via a *collocation method*. A similar technique has been used to enforce Dirichlet boundary conditions by Bertrand *et al.* [3].

Using the above finite-dimensional spaces leads to the following approximation of problem (1)–(6):

For a.e. $t > 0$, find $\mathbf{u}(t) \in W_{0,h}$, $p(t) \in L^2_{0,h}$, $\mathbf{V_G}(t) \in \mathbb{R}^2$, $\mathbf{G}(t) \in \mathbb{R}^2$, $\omega(t) \in \mathbb{R}$, $\boldsymbol{\lambda}_h(t) \in \Lambda_{0,h}(t)$ such that

$$\rho_f \int_\Omega \left[\frac{\partial \mathbf{u}_h}{\partial t} + (\mathbf{u}_h \cdot \boldsymbol{\nabla}) \mathbf{u}_h \right] \cdot \mathbf{v} \, d\mathbf{x} + \mu_f \int_\Omega \boldsymbol{\nabla} \mathbf{u}_h : \boldsymbol{\nabla} \mathbf{v} \, d\mathbf{x} - \int_\Omega p_h \boldsymbol{\nabla} \cdot \mathbf{v} \, d\mathbf{x} - \langle \boldsymbol{\lambda}_h, \mathbf{v} \rangle_{B_h(t)}$$
$$= \int_\Omega \mathbf{F} \cdot \mathbf{v} \, d\mathbf{x}, \quad \forall \mathbf{v} \in W_{0,h}, \tag{14}$$

$$\int_\Omega q \boldsymbol{\nabla} \cdot \mathbf{u}_h(t) \, d\mathbf{x} = 0, \quad \forall q \in L^2_h, \tag{15}$$

$$\langle \mu, \mathbf{u}_h(t) \rangle_{B_h(t)} = 0, \quad \forall \boldsymbol{\mu} \in \Lambda_{0,h}(t), \tag{16}$$

$$\frac{d\mathbf{G}}{dt} = \mathbf{V_G}, \tag{17}$$

$$\mathbf{V_G}(0) = \mathbf{V}^0_{\mathbf{G}}, \quad \omega(0) = \omega^0, \quad \mathbf{G}(0) = \mathbf{G}^0 = \left\{ G^0_1, G^0_2 \right\}^t, \tag{18}$$

$$\mathbf{u}_h(\mathbf{x}, 0) = \bar{\mathbf{u}}_{0,h}(\mathbf{x}) \quad (\text{with } \boldsymbol{\nabla} \cdot \bar{\mathbf{u}}_{0,h} = 0). \tag{19}$$

Applying a first-order operator splitting scheme à la Marchuk–Yanenko [19] (also see [12, 13]) to discretize Eqs. (14)–(19) in time, we obtain (after dropping some of the subscripts h)

$$\mathbf{u}^0 = \bar{\mathbf{u}}_{0,h}, \mathbf{V}^0_{\mathbf{G}}, \omega^0, \text{ and } \mathbf{G}^0 \text{ are given;} \tag{20}$$

for $n \geq 0$, knowing $\mathbf{u}^n$, $\mathbf{V}^n_{\mathbf{G}}$, ω^n and $\mathbf{G}^n$, compute $\mathbf{u}^{n+1/6}$ and $p^{n+1/6}$ via the solution of

$$\begin{aligned} &\rho_f \int_\Omega \frac{\mathbf{u}^{n+1/6} - \mathbf{u}^n}{\triangle t} \cdot \mathbf{v} \, d\mathbf{x} - \int_\Omega p^{n+1/6} \boldsymbol{\nabla} \cdot \mathbf{v} \, d\mathbf{x} = 0, \quad \forall \mathbf{v} \in W_{0,h}, \\ &\int_\Omega q \boldsymbol{\nabla} \cdot \mathbf{u}^{n+1/6} \, d\mathbf{x} = 0, \quad \forall q \in L^2_h; \quad \mathbf{u}^{n+1/6} \in W_{0,h}, \quad p^{n+1/6} \in L^2_{0,h}. \end{aligned} \tag{21}$$

Then compute $\mathbf{u}^{n+2/6}$ via the solution of

$$\int_\Omega \frac{\partial \mathbf{u}}{\partial t}\cdot \mathbf{v}\,d\mathbf{x} + \int_\Omega \big(\mathbf{u}^{n+1/6}\cdot\nabla\big)\mathbf{u}\cdot\mathbf{v}\,d\mathbf{x} = 0, \quad \forall \mathbf{v}\in W_{0,h}, \quad \text{on } (t^n, t^{n+1}),$$
$$\mathbf{u}(t^n) = \mathbf{u}^{n+1/6}; \quad \mathbf{u}(t)\in W_{0,h}, \tag{22}$$

$$\mathbf{u}^{n+2/6} = \mathbf{u}(t^{n+1}). \tag{23}$$

Next, compute $\mathbf{u}^{n+3/6}$ via the solution of

$$\rho_f \int_\Omega \frac{\mathbf{u}^{n+3/6}-\mathbf{u}^{n+2/6}}{\triangle t}\cdot\mathbf{v}\,d\mathbf{x} + \alpha\mu_f\int_\Omega \nabla\mathbf{u}^{n+3/6}\cdot\nabla\mathbf{v}\,d\mathbf{x} = 0, \forall \mathbf{v}\in W_{0,h}; \quad \mathbf{u}^{n+3/6}\in W_{0,h}. \tag{24}$$

Now predict the position and the translation velocity of the center of mass of the particles as follows:

Take $\mathbf{V}_{\mathbf{G}}^{n+\frac{4}{6},0} = \mathbf{V}_{\mathbf{G}}^{n}$ and $\mathbf{G}^{n+\frac{4}{6},0} = \mathbf{G}^n$; then predict the new position of the particle via the following subcycling and predicting–correcting technique:

For $k = 1, \ldots, N$, compute

$$\hat{\mathbf{V}}_{\mathbf{G}}^{n+\frac{4}{6},k} = \mathbf{V}_{\mathbf{G}}^{n+\frac{4}{6},k-1} + \mathbf{F}^r\big(\mathbf{G}^{n+\frac{4}{6},k-1}\big)\triangle t/2N, \tag{25}$$

$$\hat{\mathbf{G}}^{n+\frac{4}{6},k} = \mathbf{G}^{n+\frac{4}{6},k-1} + \Big(\hat{\mathbf{V}}_{\mathbf{G}}^{n+\frac{4}{6},k} + \mathbf{V}_{\mathbf{G}}^{n+\frac{4}{6},k-1}\Big)\triangle t/4N, \tag{26}$$

$$\mathbf{V}_{\mathbf{G}}^{n+\frac{4}{6},k} = \mathbf{V}_{\mathbf{G}}^{n+\frac{4}{6},k-1} + \big(\mathbf{F}^r\big(\hat{\mathbf{G}}^{n+\frac{4}{6},k}\big) + \mathbf{F}^r\big(\mathbf{G}^{n+\frac{4}{6},k-1}\big)\big)\triangle t/4N, \tag{27}$$

$$\mathbf{G}^{n+\frac{4}{6},k} = \mathbf{G}^{n+\frac{4}{6},k-1} + \Big(\mathbf{V}_{\mathbf{G}}^{n+\frac{4}{6},k} + \mathbf{V}_{\mathbf{G}}^{n+\frac{4}{6},k-1}\Big)\triangle t/4N, \tag{28}$$

enddo;

and let $\mathbf{V}_{\mathbf{G}}^{n+\frac{4}{6}} = \mathbf{V}_{\mathbf{G}}^{n+\frac{4}{6},N}, \quad \mathbf{G}^{n+\frac{4}{6}} = \mathbf{G}^{n+\frac{4}{6},N}.$ (29)

Now, compute $\mathbf{u}^{n+5/6}$, $\boldsymbol{\lambda}^{n+5/6}$, $\mathbf{V}_{\mathbf{G}}^{n+5/6}$, and $\omega^{n+5/6}$ via the solution of

$$\rho_f\int_\Omega \frac{\mathbf{u}^{n+5/6}-\mathbf{u}^{n+3/6}}{\triangle t}\cdot\mathbf{v}\,d\mathbf{x} + \beta\mu_f\int_\Omega \nabla\mathbf{u}^{n+5/6}\cdot\nabla\mathbf{v}\,d\mathbf{x} = \langle\boldsymbol{\lambda},\mathbf{v}\rangle_{B_h^{n+4/6}}, \quad \forall\mathbf{v}\in W_{0,h},$$
$$\big\langle\boldsymbol{\mu},\mathbf{u}^{n+5/6}\big\rangle_{B_h^{n+4/6}} = 0, \quad \forall\boldsymbol{\mu}\in\Lambda_{0,h}^{n+4/6}; \quad \mathbf{u}^{n+5/6}\in W_{0,h}, \quad \boldsymbol{\lambda}^{n+5/6}\in\Lambda_{0,h}^{n+4/6}, \tag{30}$$

and solve for $\mathbf{V}_{\mathbf{G}}^{n+5/6}$ and $\omega^{n+5/6}$ from

$$\big\langle\mathbf{e}_i,\mathbf{u}^{n+5/6}-\mathbf{V}_{\mathbf{G}}^{n+5/6}-\omega^{n+5/6}\overrightarrow{G^{n+4/6}x}^{\perp}\big\rangle_{B_h^{n+4/6}} = 0, \quad \text{for } i=1,2,$$
$$\big\langle\overrightarrow{G^{n+4/6}x}^{\perp},\mathbf{u}^{n+5/6}-\mathbf{V}_{\mathbf{G}}^{n+5/6}-\omega^{n+5/6}\overrightarrow{G^{n+4/6}x}^{\perp}\big\rangle_{B_h^{n+4/6}} = 0, \tag{31}$$

Finally, take $\mathbf{V}_{\mathbf{G}}^{n+1,0} = \mathbf{V}_{\mathbf{G}}^{n+5/6}$ and $\mathbf{G}^{n+1,0} = \mathbf{G}^{n+4/6}$; then predict the final position and translation velocity as follows:

For $k = 1, \ldots, N,$ compute (32)

$$\hat{\mathbf{V}}_{\mathbf{G}}^{n+1,k} = \mathbf{V}_{\mathbf{G}}^{n+1,k-1} + \mathbf{F}^r(\mathbf{G}^{n+1,k-1})\triangle t/2N, \tag{33}$$

$$\hat{\mathbf{G}}^{n+1,k} = \mathbf{G}^{n+1,k-1} + \big(\hat{\mathbf{V}}_{\mathbf{G}}^{n+1,k} + \mathbf{V}_{\mathbf{G}}^{n+1,k-1}\big)\triangle t/4N, \tag{34}$$

$$\mathbf{V}_{\mathbf{G}}^{n+1,k} = \mathbf{V}_{\mathbf{G}}^{n+1,k-1} + (\mathbf{F}^r(\hat{\mathbf{G}}^{n+1,k}) + \mathbf{F}^r(\mathbf{G}^{n+1,k-1}))\triangle t/4N, \tag{35}$$

$$\mathbf{G}^{n+1,k} = \mathbf{G}^{n+1,k-1} + \big(\mathbf{V}_{\mathbf{G}}^{n+1,k} + \mathbf{V}_{\mathbf{G}}^{n+1,k-1}\big)\triangle t/4N,$$

enddo;

and let $\mathbf{V}_{\mathbf{G}}^{n+1} = \mathbf{V}_{\mathbf{G}}^{n+1,N}$, $\mathbf{G}^{n+1} = \mathbf{G}^{n+1,N}$; and set $\mathbf{u}^{n+1} = \mathbf{u}^{n+5/6}$, $\omega^{n+1} = \omega^{n+5/6}$.

In above algorithm (20)–(35), we have $t^{n+s} = (n+s)\triangle t$, $\Lambda_{0,h}^{n+s} = \Lambda_{0,h}(t^{n+s})$, B_h^{n+s} is the region occupied by the particle centered at $\mathbf{G}^{n+s}$, and $\mathbf{F}^r$ is a short-range repulsion force which prevents the particle/particle and particle/wall penetration (see, e.g., [12, 13]). Finally, α and β verify $\alpha + \beta = 1$; we have chosen $\alpha = 1$ and $\beta = 0$ in the numerical simulations discussed later.

3.1. *Solutions of the Subproblems* (21), (22), (24), *and* (30)

The degenerated quasi-Stokes problem (21) is solved by a preconditioned conjugate gradient method introduced in [11], in which discrete elliptic problems from the preconditioning are solved by a matrix-free fast solver from FISHPAK by Adams *et al.* in [1]. The advection problem (22) for the velocity field is solved by a wave-like equation method as in [7, 22]. Problem (24) is a classical discrete elliptic problem which can be solved by the same matrix-free fast solver.

To enforce the rigid body motion inside the region occupied by the particles, we have to modify the conjugate gradient method discussed in [12] since at each iteration we have to project the distributed Lagrange multiplier back to the finite-dimensional subspace of $\Lambda_0(t)$. The saddle point problem (30) is a particular case of

$$\begin{aligned} \alpha \int_\Omega \mathbf{u}\cdot\mathbf{v}\,d\mathbf{x} + \mu \int_\Omega \boldsymbol{\nabla}\mathbf{u} : \boldsymbol{\nabla}\mathbf{v}\,d\mathbf{x} &= \int_\Omega \mathbf{f}\cdot\mathbf{v}\,d\mathbf{x} + \langle \boldsymbol{\lambda}, \mathbf{v}\rangle_{B_h^s}, \quad \forall \mathbf{v} \in W_{0,h}, \\ \langle \boldsymbol{\mu}, \mathbf{u}\rangle_{B_h^s} = 0, \quad \forall \boldsymbol{\mu} \in \Lambda_{0,h}^s; \quad \mathbf{u} \in W_{0,h}, \quad \boldsymbol{\lambda} &\in \Lambda_{0,h}^s. \end{aligned} \tag{36}$$

The modified conjugate gradient method for the solution of (36) reads as follows:

$$\boldsymbol{\lambda}^0 \in \Lambda_{0,h}^s \text{ is given,} \tag{37}$$

solve

$$\alpha \int_\Omega \mathbf{u}^0\cdot\mathbf{v}\,d\mathbf{x} + \mu \int_\Omega \boldsymbol{\nabla}\mathbf{u}^0 : \boldsymbol{\nabla}\mathbf{v}\,d\mathbf{x} = \int_\Omega \mathbf{f}\cdot\mathbf{v}\,d\mathbf{x} + \langle \boldsymbol{\lambda}^0, \mathbf{v}\rangle_{B_h^s}, \quad \forall \mathbf{v} \in W_{0,h}; \quad \mathbf{u}^0 \in W_{0,h}; \tag{38}$$

then solve

$$\langle \boldsymbol{\mu}, \mathbf{g}^0\rangle_{B_h^s} = \langle \boldsymbol{\mu}, \mathbf{u}^0\rangle_{B_h^s}, \quad \forall \boldsymbol{\mu} \in \Lambda_{0,h}^s, \tag{39}$$

and set

$$\mathbf{w}^0 = \mathbf{g}^0. \tag{40}$$

For $m \geq 0$, assuming that $\boldsymbol{\lambda}^m$, $\mathbf{u}^m$, $\mathbf{w}^m$, $\mathbf{g}^m$ are known, compute $\boldsymbol{\lambda}_h^{m+1}$, $\mathbf{u}^{m+1}$, $\mathbf{w}^{m+1}$, $\mathbf{g}^{m+1}$ as follows:
Solve

$$\alpha \int_\Omega \bar{\mathbf{u}}^m \cdot \mathbf{v}\, d\mathbf{x} + \mu \int_\Omega \boldsymbol{\nabla} \bar{\mathbf{u}}^m : \boldsymbol{\nabla} \mathbf{v}\, d\mathbf{x} = \langle \mathbf{w}^m, \mathbf{v} \rangle_{B_h^s}, \quad \forall \mathbf{v} \in W_{0,h}; \quad \bar{\mathbf{u}}^m \in W_{0,h}, \tag{41}$$

and set

$$\langle \boldsymbol{\mu}, \bar{\mathbf{g}}^m \rangle_{B_h^s} = \langle \boldsymbol{\mu}, \bar{\mathbf{u}}^m \rangle_{B_h^s}, \quad \forall \boldsymbol{\mu} \in \Lambda_{0,h}^s. \tag{42}$$

Then compute

$$\rho_m = \langle \mathbf{g}^m, \mathbf{g}^m \rangle_{B_h^s} / \langle \mathbf{w}^m, \bar{\mathbf{u}}^m \rangle_{B_h^s}, \tag{43}$$

and set

$$\boldsymbol{\lambda}^{m+1} = \boldsymbol{\lambda}^m - \rho_m \mathbf{w}^m, \tag{44}$$

$$\mathbf{u}^{m+1} = \mathbf{u}^m - \rho_m \bar{\mathbf{u}}^m, \tag{45}$$

$$\mathbf{g}^{m+1} = \mathbf{g}^m - \rho_m \bar{\mathbf{g}}^m. \tag{46}$$

If $\langle \mathbf{g}^{m+1}, \mathbf{g}^{m+1} \rangle_{B_h^s} / \langle \mathbf{g}^0, \mathbf{g}^0 \rangle_{B_h^s} \leq \epsilon$, then take $\mathbf{u} = \mathbf{u}^{m+1}$. If not, compute

$$\gamma_m = \langle \mathbf{g}^{m+1}, \mathbf{g}^{m+1} \rangle_{B_h^s} / \langle \mathbf{g}^m, \mathbf{g}^m \rangle_{B_h^s}, \tag{47}$$

and set

$$\mathbf{w}^{m+1} = \mathbf{g}^{m+1} + \gamma_m \mathbf{w}^m. \tag{48}$$

Do $m = m + 1$ and go back to (41).

Remark 4. In (39) and (42), we compute

$$\langle \boldsymbol{\mu}, \mathbf{g} \rangle_{B_h^s} = \langle \boldsymbol{\mu}, \mathbf{u} \rangle_{B_h^s}, \quad \forall \boldsymbol{\mu} \in \Lambda_{0,h}^s \tag{49}$$

as follows: Find first $\tilde{\mathbf{g}} \in \Lambda_h^s$ so that

$$\langle \boldsymbol{\mu}, \tilde{\mathbf{g}} \rangle_{B_h^s} = \langle \boldsymbol{\mu}, \mathbf{u} \rangle_{B_h^s}, \quad \forall \boldsymbol{\mu} \in \Lambda_h^s \tag{50}$$

and then project $\tilde{\mathbf{g}}$ into $\Lambda_{0,h}^s$ by finding c_0, c_1, and c_2 so that

$$\mathbf{g} = \tilde{\mathbf{g}} - c_1 \mathbf{e}_1 - c2\mathbf{e}_2 - c_0 \overrightarrow{Gx}^\perp, \tag{51}$$

satisfies

$$\langle \mathbf{g}, \mathbf{e}_i \rangle_{B_h^s} = 0, \quad \text{for } i = 1, 2, \quad \langle \mathbf{g}, \overrightarrow{Gx}^\perp \rangle_{B_h^s} = 0. \tag{52}$$

4. NUMERICAL EXPERIMENTS AND DISCUSSION

4.1. *One and Several Circular Cylinder Cases*

In the first test case, we consider the simulation of the motion of a neutrally buoyant particle in a pressure-driven Poiseuille flow. This case was considered by Inamuro *et al.* in [15]; their results were obtained via a lattice Boltzmann method. Here we have used the same sets of parameters (except time step) to validate our method. The computational domain is $\Omega = (0, 1) \times (0, 1)$, implying that the height D of the channel is 1. The flow velocity is periodic in the x_1 (horizontal) direction and zero at the top and bottom of the domain. A pressure drop is given (see Table I) for each case so that the flow moves from the left to the right. The initial flow velocity and particle velocities are at rest. The initial x_2 coordinate of the center of the circular cylinder is 0.4. The densities of the fluid and of the particles are 1 and the viscosity μ_f of the fluid varies (see Table I). The particle diameter is 0.25. We have used structured triangular meshes in all simulations. Here the mesh size for the velocity field is $h_v = 1/200$. The mesh size for the pressure is $h_p = 2h_v$. The time step is chosen to be $\triangle t = 0.002$.

In Table I the space-averaged inlet velocity $\bar{u}$, the equilibrium position of the circular cylinder, and the angular velocity are at most 1.16%, 0.6%, and 2.1%, respectively, from the values in [15]. (The averaged value $\bar{u}^*$ in [15] was preferable due to the errors in their computation proportional to $(\bar{u}^*)^2$.) Figure 4 shows the lateral migration curves of the circular cylinder from the same initial position at different Reynolds numbers, namely $\mathrm{Re} = 12.78, 27.73$, and 96.74 ($\mathrm{Re} = D\bar{u}/\mu_f$). In the sixth case, the equilibrium position of the circular cylinder is slightly closer to the center axis of the channel than in the fifth case. We believe it is possible due to the higher flow rate; actually similar results also occurred in the experiments shown in [21], in which the ball is closer to the center of the tube at higher flow rate.

In the second case, we consider the simulation of the motions of eight neutrally buoyant circular cylinders in a pressure-driven Poiseuille flow, which are lined up along a vertical line initially (see Fig. 5). The computational domain is $\Omega = (0, 42) \times (0, 12)$, implying that the height D of the channel is 12. The initial flow velocity and particle velocities are zeros. The pressure drop is $dp = 25/18$ so that the maximum horizontal speed is 25

TABLE I

Parameters for Each Computation (in Columns 1 and 2) and Comparisons (in Columns 3–8) between the Computed Results and the Ones in [15]

μ_f	$\triangle p$	$\bar{u}^*$	$\bar{u}$	x_2^{c*}	x_2^c	ω^*	ω
3.2498036×10^{-3}	1.763×10^{-3}	0.04137	0.04155	0.2745	0.2732	−0.054675	−0.05345
1.5000000×10^{-3}	8.167×10^{-4}	0.04131	0.04159	0.2733	0.2725	−0.054694	−0.05343
9.4984908×10^{-4}	5.133×10^{-4}	0.04091	0.04122	0.2728	0.2723	−0.053772	−0.05264
7.5000000×10^{-4}	4.100×10^{-4}	0.04118	0.04166	0.2723	0.2720	−0.053765	−0.05283
6.0000000×10^{-4}	3.270×10^{-4}	0.04110	0.04148	0.2716	0.2719	−0.053101	−0.05206
4.2834760×10^{-4}	2.337×10^{-4}	0.04101	0.04144	0.2706	0.2722	−0.051607	−0.05052

Notes. μ_f is the viscosity of the fluid, $\triangle p$ is the pressure drop, $\bar{u}$ is the space-averaged velocity at the inlet ($x_1 = 0$) after the circular disk reaches the equilibrium position, x_2^c is the equilibrium position, ω is the angular speed after the circular disk reaches the equilibrium position, and those with * are obtained from [15].

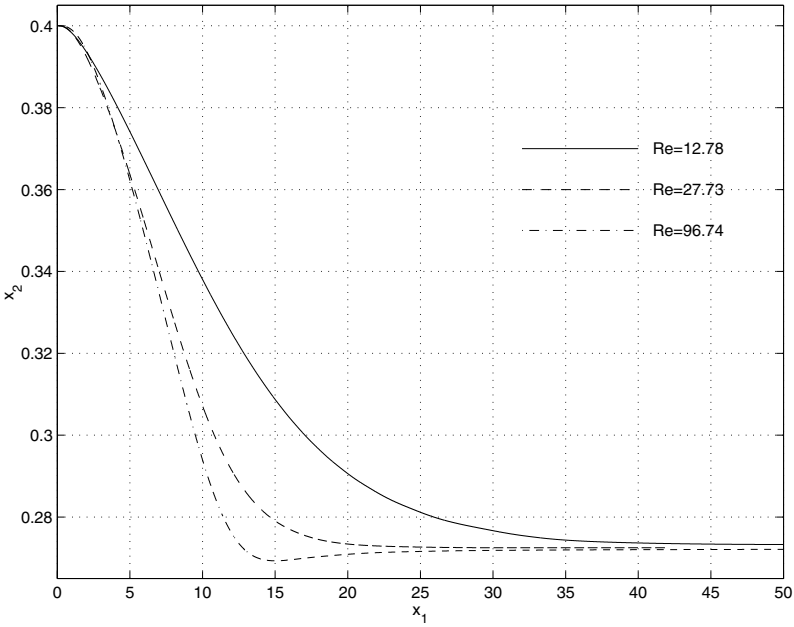

FIG. 4. Lateral migrations of a circular cylinder at different Reynolds numbers.

when there is no particle (hence μ_f is 1). The densities of the fluid and of the particles are 1. The particle diameter d is 0.9. The mesh size for the velocity field is $h_v = 1/10$. The mesh size for the pressure is $h_p = 2h_v$. The time step is $\triangle t = 0.001$. At $t = 200$, the space-averaged velocity $\bar{u}$ is 16.33 and the averaged particle speed $\bar{u}_p$ is 18.12. Hence the Reynolds

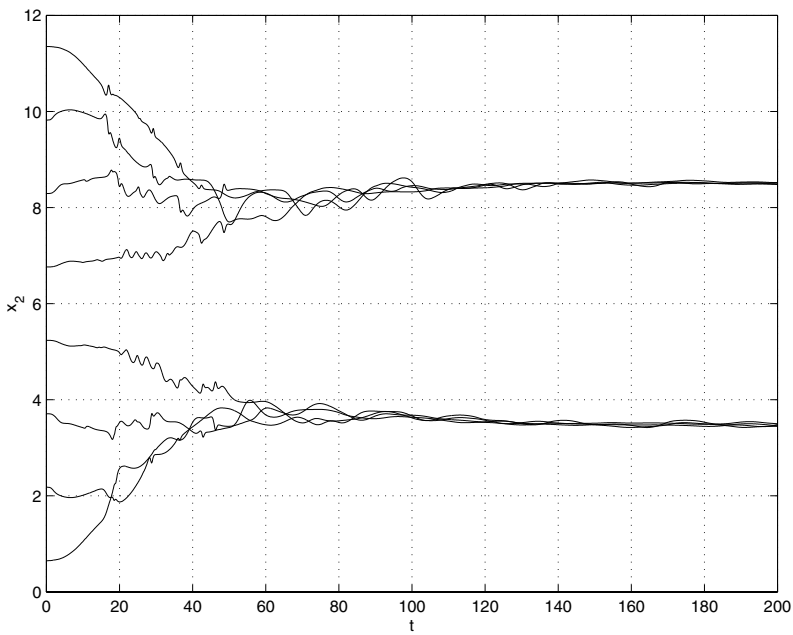

FIG. 5. Lateral migration curves of eight circular cylinders from different initial positions.

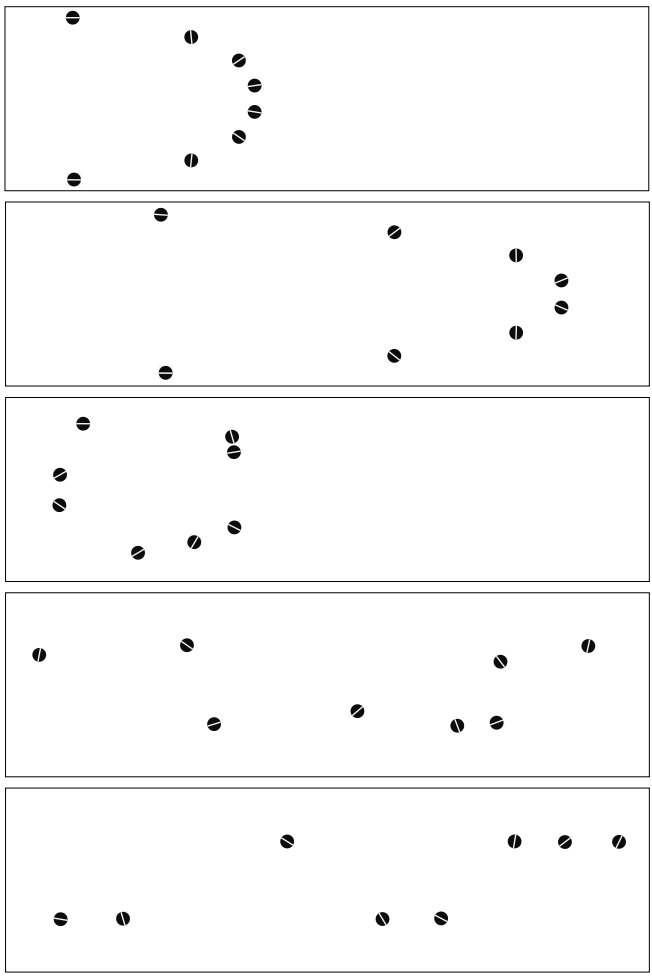

FIG. 6. The eight particle positions at $t = 5$, 7.5, 20, 40, and 200 (from top to bottom).

number $\mathrm{Re} = \bar{u}D/\mu_f$ is 195.96 and the averaged particle Reynolds number $\mathrm{Re} = \bar{u}_p d/\mu_f$ is 16.308. The lateral migration curves of eight circular cylinders with respect to time from the different initial positions simultaneously are shown in Fig. 5. Figure 6 shows that particles interact among themselves before they reach the equilibrium positions.

In the third case, we simulate the motions of 56 neutrally buoyant circular cylinders in a pressure-driven Poiseuille flow, which was considered in [14]. The computational domain is $\Omega = (0, 21) \times (0, 10)$. The initial flow velocity and particle velocities are zeros. The pressure drop is $dp = 2$ and μ_f is 1 so that the maximum horizontal speed is 25 when there is no particle. The densities of the fluid and of the particles are 1. The particle diameter d is 1. The mesh size for the velocity field is $h_v = 1/8$. The mesh size for the pressure is $h_p = 2h_v$. The time step is $\triangle t = 0.001$. At $t = 40$, the maximum particle velocity is 14.76 near the centerline and the maximum fluid velocity without particles is 25 so the maximum slip velocity is 10.24 near the centerline. In [14] at $t = 39.75$ the maximum particle velocity is 15 near the centerline and the maximum slip velocity is 10. The agreement of the results obtained by two different methods is very good. The velocity profile of the fluid without particles and the velocities of the particles at $t = 30$ and 40 are shown in Fig. 7.

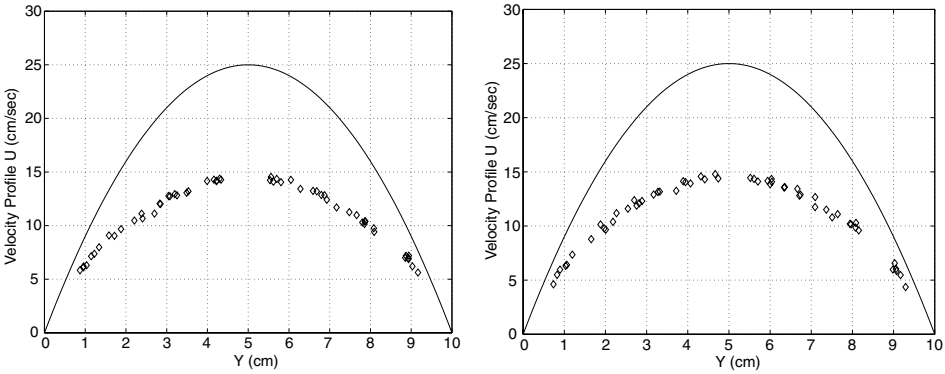

FIG. 7. The velocity profile of the fluid without particles and the velocities of 56 particles at $t = 30$ (left) and 40 (right).

4.2. *Many Circular Disk Cases*

We consider the simulation of the motion of hundreds of neutrally buoyant particles in a pressure-driven Poiseuille flow. The computational domain is $\Omega = (0, 42) \times (0, 12)$. The flow velocity is periodic in the horizontal direction and zero at the top and bottom of the domain. A fixed horizontal force is given for all cases so that the flow moves from the left to the right (and the maximum horizontal speed is 25 when there is no particle). The initial flow velocity and particle velocities are at rest. The densities of the fluid and the particles are 1 and the viscosity of the fluid is 1. In the first two cases there are 240 and 300 neutrally buoyant particles of diameter 0.9, respectively. In the third case, there are 1200 neutrally buoyant particles of diameter 0.45. The initial position of the particles is arranged like a rectangular lattice shown in Fig. 8. We have used structured triangular meshes in all simulations. The mesh size for the velocity field is $h_v = 1/10$ for the first two cases and $h_v = 1/20$ for the third case. The mesh size for pressure is $h_p = 2h_v$. The time step is $\triangle t = 0.001$.

In the case of 240 particles we observed that particles move away from the center in Fig. 8 at the beginning and at $t = 40$ the symmetry breaking have already occurred since not only the angles of the particles in the second and the seventh rows are quite different, but also the relative position of the particles are not symmetric. One of the possible reasons is that the mesh is not symmetric with respect to the central line of the channel. The central horizontal gap size at $t = 60$ is 1.514 times the one at $t = 0$. Then the basic two particle interaction (see Fortes *et al.* [10]), *drafting, kissing*, and *tumbling*, occurred around $t = 63$ and the pattern of the stable horizontal lines of particles was destroyed. The 240 particle positions at $t = 150$, 300, and 320 are shown in Fig. 9. The distribution of the average solid fraction from $t = 300$ to 320 is shown in Fig. 10. The solid fraction for the 240 particle case is 30.29%. The maximum horizontal speed of the particles is about 13.14, 13.09, and 12.09 at $t = 60$, 65, and 320, respectively.

Similar results are also obtained in the case of 300 particles. The central horizontal gap size at $t = 70$ is 1.76 times the initial size (see Fig. 11). The distribution of the average solid fraction from $t = 680$ to 700 is shown in Fig. 12. The solid fraction for this 300 particle case is 37.86%. The maximum horizontal speed of the particles is about 10.17 and 10.04 at $t = 70$ and 700, respectively.

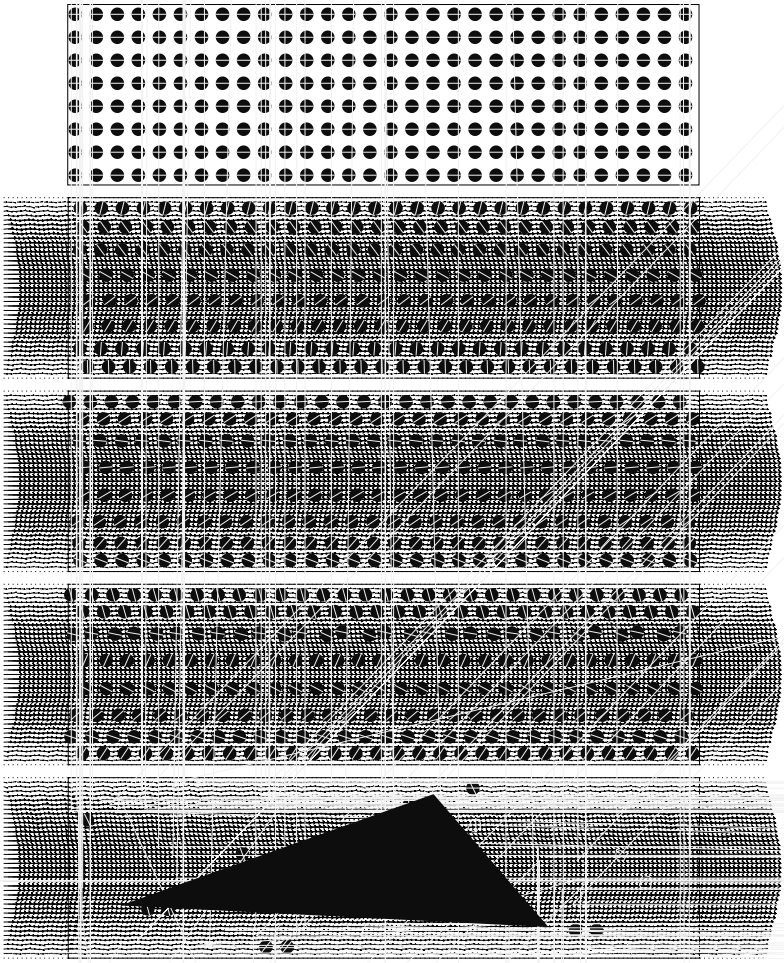

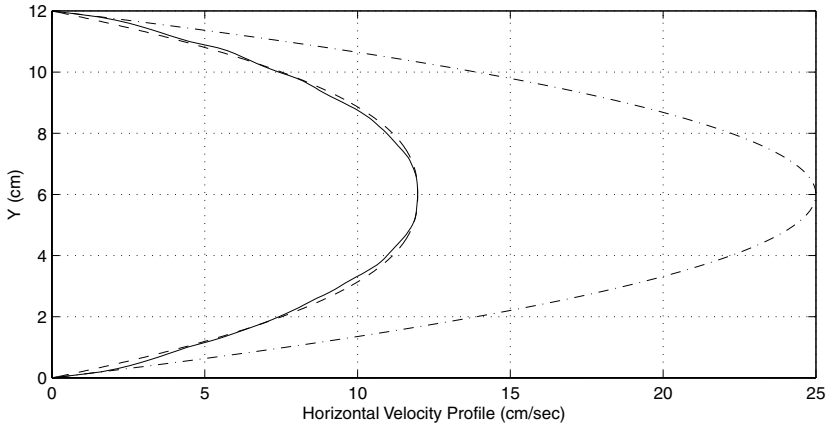

FIG. 15. Velocity profile of the flow without particles (dashed–dotted line), averaged horizontal velocity of flow (solid line), and the profile of the power law solution (dashed line) for the case of 240 neutrally buoyant particles at $t = 320$ with $dp = 1.3\bar{8}$, $Q = 101.85$, $U_{max} = 11.967$, $s = 0.695$, and $\mu_e = 2.77677$.

Here we solve an inverse problem. Once we know the flow rate Q and the maximal speed U_{max} from the simulations, we obtain the exponent from

$$s = (Q - HU_{max})/(HU_{max} - 2Q) \tag{57}$$

and the effective viscosity by

$$\mu_e = dp \Big/ \left(\frac{(s+1)\, U_{max}}{s(H/2)^{(s+1)/s}} \right)^s. \tag{58}$$

To get Q, we first computed the flow rate along each vertical mesh line in the computational domain and then averaged them to get the averaged flow rate for Q even though the flow rate along each vertical line varies less than one tenth of a percent of the averaged value. To get

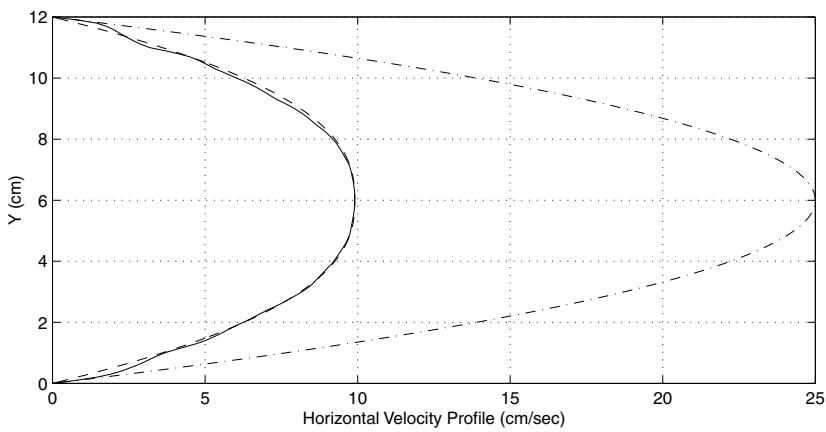

FIG. 16. Velocity profile of the flow without particles (dashed–dotted line), averaged horizontal velocity of flow (solid line), and the profile of the power law solution (dashed line) for the case of 300 neutrally buoyant particles at $t = 700$, $dp = 1.3\bar{8}$, $Q = 84.67$, $U_{max} = 9.907$, $s = 0.678$, and $\mu_e = 3.20888$.

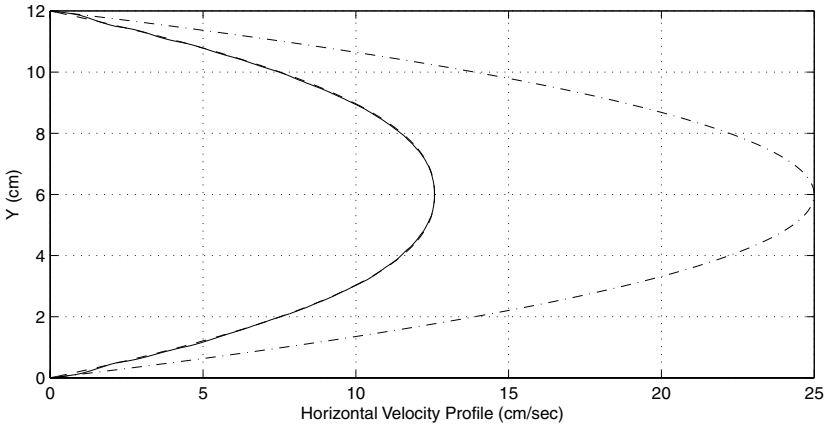

FIG. 17. Velocity profile of the flow without particles (dashed–dotted line), averaged horizontal velocity of flow (solid line), and the profile of the power law solution (dashed line) for the case of 1200 neutrally buoyant particles at $t = 400$, $dp = 1.3\bar{8}$, $Q = 104.47$, $U_{max} = 12.575$, $s = 0.799$, and $\mu_e = 2.41081$.

U_{max}, we computed the averaged horizontal velocity along each horizontal mesh line in the computational domain and then found the maximum among them. With the calculated Q and U_{max}, we got the exponent s by (57) and the effective viscosity by (58). In Figs. 15–17 we have shown the exponents and the effective viscosities associated with the simulations presented in the previous section. In Fig. 16, the curve of averaged horizontal velocity is slightly off the curve of power law solution due to a layer of circular cylinders next to each wall. But in Fig. 17 for the case with 1200 smaller circular cylinders, they match remarkably well.

ACKNOWLEDGMENTS

We acknowledge the helpful comments and suggestions of E. J. Dean, J. He, H. H. Hu, P. Huang, D. D. Joseph, Y. Kuznetsov, G. Rodin, and referees. We acknowledge also the support of NSF (Grants ECS-9527123, CTS-9873236, DMS-9973318, and CCR-9902035), Texas Board of Higher Education (ARP Grant 003652-0383-1999), and DOE/LASCI (Grant R71700K-292-000-99).

REFERENCES

1. J. Adams, P. Swarztrauber, and R. Sweet, *FISHPAK: A Package of Fortran Subprograms for the Solution of Separable Elliptic Partial Differential Equations* (The National Center for Atmospheric Research, Boulder, 1980).
2. E. S. Asmolov, The inertial lift on a spherical particle in a plane Poiseuille flow at large channel number, *J. Fluid Mech.* **381**, 63 (1999).
3. T. Bertrand, P. A. Tanguy, and F. Thibault, A three-dimensional fictitious domain method for incompressible fluid flow problem, *Int. J. Numer. Meth. Fluids* **25**, 719 (1997).
4. H. Brenner, Hydrodynamic resistance of particles at small Reynolds numbers, *Adv. Chem. Eng.* **6**, 287 (1966).
5. M. O. Bristeau, R. Glowinski, and J. Periaux, Numerical methods for the Navier–Stokes equations: Applications to the simulation of compressible and incompressible viscous flow, *Comput. Phys. Rep.* **6**, 73 (1987).
6. R. G. Cox and S. G. Mason, Suspended particles in fluid flow through tubes, *Annu. Rev. Fluid Mech.* **3**, 291 (1971).

7. E. J. Dean and R. Glowinski, A wave equation approach to the numerical solution of the Navier–Stokes equations for incompressible viscous flow, *C.R. Acad. Sci. Paris, Sér. 1* **325**, 789 (1997).
8. J. Feng, H. H. Hu, and D. D. Joseph, Direct simulation of initial value problems for the motion of solid bodies in a Newtonian fluid. Part 2: Couette and Poiseuille flows, *J. Fluid Mech.* **277**, 271 (1994).
9. F. Feuillebois, Some theoretical results for the motion of solid spherical particles in a viscous fluid, in *Multiphase Science and Technology*, edited by G. F. Hewitt, J. M. Delhaye, and N. Zuber (Hemisphere, New York, 1989), Vol. 4, p. 583.
10. A. F. Fortes, D. D. Joseph, and T. S. Lundgren, Nonlinear mechanics of fluidization of beds of spherical particles, *J. Fluid Mech.* **177**, 467 (1987).
11. R. Glowinski, T.-W. Pan, and J. Periaux, Distributed Lagrange multiplier methods for incompressible flow around moving rigid bodies, *Comput. Meth. Appl. Mech. Eng.* **151**, 181 (1998).
12. R. Glowinski, T.-W. Pan, T. Hesla, and D. D. Joseph, A distributed Lagrange multiplier/fictitious domain method for particulate flows, *Int. J. Multiphase Flow* **25**, 755 (1999).
13. R. Glowinski, T.-W. Pan, T. Hesla, D. D. Joseph, and J. Periaux, A fictitious domain approach to the direct numerical simulation of incompressible viscous flow past moving rigid bodies: Application to particulate flow, *J. Comput. Phys.* **169**, 363 (2001).
14. P. Y. Huang and D. D. Joseph, Effects of shear thinning on migration of neutrally buoyant particles in pressure driven flow of Newtonian and viscoelastic fluids, *J. Non-Newtonian Fluid Mech.* **90**, 159 (2000).
15. T. Inamuro, K. Maeba, and F. Ogino, Flow between parallel walls containing the lines of neutrally buoyant circular cylinders, *Int. J. Multiphase Flow* **26**, 1981 (2000).
16. A. Karnis, H. L. Goldsmith, and S. G. Mason, The flow of suspensions through tubes. Part V: Inertial effects, *Can. J. Chem. Eng.* **44**, 181 (1966).
17. L. G. Leal, Particle motions in viscous, *Annu. Rev. Fluid Mech.* **12**, 435 (1980).
18. D. Leighton and A. Acrivos, The shear-induced migration of particles in concentrated suspensions, *J. Fluid Mech.* **181**, 415 (1987).
19. G. I. Marchuk, Splitting and alternating direction methods, in *Handbook of Numerical Analysis*, edited by P. G. Ciarlet and J. L. Lions (North-Holland, Amsterdam, 1990), Vol. I, p. 197.
20. J. F. Morris and J. F. Brady, Pressure-driven flow of a suspension: Buoyancy effects, *Int. J. Multiphase Flow* **24**, 105 (1998).
21. D. R. Oliver, Influence of particle rotation on radial migration in the Poiseuille flow of suspensions, *Nature* **194**, 1269 (1962).
22. T.-W. Pan and R. Glowinski, A projection/wave-like equation method for the numerical simulation of incompressible viscous fluid flow modeled by the Navier–Stokes equations, *Comput. Fluid Dyn. J.* **9**, 28 (2000).
23. G. Segré and A. Silberberg, Radial particle displacements in Poiseuille flow of suspensions, *Nature* **189**, 209 (1961).
24. G. Segré and A. Silberberg, Behavior of macroscopic rigid spheres in Poiseuille flow: Part I, *J. Fluid Mech.* **14**, 115 (1962).